



## Article

# Spatial Characteristics of Aeolian Sand Transport Affected by Surface Vegetation along the Oshang Railway

Ning Huang <sup>1,2</sup>, Yanhong Song <sup>1,2</sup> , Xuanmin Li <sup>3,\*</sup>, Bin Han <sup>3</sup>, Lihang Xu <sup>1,2</sup> and Jie Zhang <sup>1,2,\*</sup> 

<sup>1</sup> College of Civil Engineering and Mechanics, Lanzhou University, Lanzhou 730000, China; huangn@lzu.edu.cn (N.H.); songyh20@lzu.edu.cn (Y.S.); xulh21@lzu.edu.cn (L.X.)

<sup>2</sup> Key Laboratory of Mechanics on Disaster and Environment in Western China, Ministry of Education of China, Lanzhou 730000, China

<sup>3</sup> Zhengzhou Design Institute, China Railway Engineering Design and Consulting Group Co., Ltd., Zhengzhou 450001, China; ztsyyhb@163.com

\* Correspondence: lxm40434@163.com (X.L.); zhang-j@lzu.edu.cn (J.Z.)

**Abstract:** Blown sand transport plays a pivotal role in determining the optimal placement of sand protection facilities along railways in sandy areas. Surface vegetation cover significantly influences blowing sand activities along the Oshang Railway (from Otog Front Banner to Shanghai-Temple Town). In this study, the spatial characteristics of aeolian sand transport along the railway were derived from field observations conducted at five different locations, each with varying fractional vegetation cover (FVC). The results indicate that sand-transport intensity does not fully correlate with the wind energy environment, primarily due to differences in surface vegetation cover among the observation sites. We utilize the dimensionless ratio  $Q \cdot g \cdot f / (0.136 \times DP \cdot \rho_a)$  to represent the sand transport rate ( $Q$ ), the sand-moving wind frequency ( $f$ ) and drift potential ( $DP$ ), exhibiting a negative exponential trend with FVC. Sand transport is effectively restrained when FVC is greater than or equal to 20%. Conversely, when FVC is less than 20%, sand transport intensity exponentially increases with decreasing fractional vegetation cover. After careful analysis, we propose a simple empirical expression that incorporates the influence of both the wind field and fractional vegetation cover to assess sand transport on a flat surface. The study offers valuable insights for designing wind-blown sand protection measures along railways and evaluating wind-blown sand movement on a flat surface affected by vegetation.

**Keywords:** Oshang Railway; aeolian sand transport; vegetation cover; spatial distribution; field observation



**Citation:** Huang, N.; Song, Y.; Li, X.; Han, B.; Xu, L.; Zhang, J. Spatial Characteristics of Aeolian Sand Transport Affected by Surface Vegetation along the Oshang Railway. *Sustainability* **2024**, *16*, 3940. <https://doi.org/10.3390/su16103940>

Academic Editor: Elzbieta Macioszek

Received: 2 April 2024

Revised: 30 April 2024

Accepted: 6 May 2024

Published: 8 May 2024



**Copyright:** © 2024 by the authors. Licensee MDPI, Basel, Switzerland. This article is an open access article distributed under the terms and conditions of the Creative Commons Attribution (CC BY) license (<https://creativecommons.org/licenses/by/4.0/>).

## 1. Introduction

The Oshang Railway lies on the border of the Mu Us desert [1] in China's Inner Mongolia Autonomous Region [2]. This area frequently experiences high wind speeds, with 25–30 windy days (equivalent to or greater than grade 8 wind [3]) occurring mainly in spring (March–May) each year. The region's climate is arid, characterized by significant evaporation, averaging about 2462 mm annually, while rainfall is sparse and concentrated, averaging approximately 264 mm annually. Over recent years, certain areas have witnessed varying degrees of degradation in herbaceous plants due to both human activities [4] and a dry climate [5,6]. Consequently, some sand sources have gradually become exposed, creating a patchy landscape with interspersed grass and sandy areas (see Figure 1). This transformation can trigger intense blowing sand movement, leading to wind-sand disasters that threaten both human livelihoods and the ecological environment [7–10]. They can cause damage to infrastructure such as transportation [7,8] and power facilities [9]. For example, a wind-sand disaster on the Oshang Railway poses potential hazards to the ecological environment [10] and safe railway operations [11,12]. This not only affects

people's traveling activities and daily life but may also be an obstacle to the sustainable economic and ecological development of the region.



**Figure 1.** Evolution of desertification along the Oshang Railway.

To mitigate wind-sand disasters along the railway, it is imperative to establish a rational sand-control system for the railway [13–16], considering the spatial distribution characteristics of local aeolian sand transport [12]. Researchers have proposed several effective sand-control measures [17–19], including plant-based measures [20–22] and engineering-protection measures [23,24]. These measures have shown positive effects on sand-blocking and stabilization [17,18]. Although the fundamental principles of protection measures have been outlined [13,19,25–32], a practical solution for the sand-protection system of railways still needs to be established based on local sand-transport information [11,12,25]. Unfortunately, there is insufficient information available on blown sand transport along the Oshang Railway. This lack of data complicates the guidance for on-site construction of sand-control measures in the region. Therefore, we conducted field observations of wind and aeolian sand transport and quantitatively assessed blown-sand activities in the area.

Researchers have typically utilized Fryberger's approach [33,34] to quantitatively assess sand transport intensity. This method utilizes wind field data to evaluate sand transport intensity and proves particularly effective for loose, flat sandy surfaces [34]. However, it disregards surface properties, leading to a significant discrepancy between the drift potential ( $DP$ ) and actual sand transport  $Q$  [35]. To address this, Wasson et al. proposed two modified versions of Bagnold's equations [36] to describe blown sand transport influenced by shrub vegetation [36]. The modified equation one assumes that vegetation cover reduces surface wind speed without altering the critical wind speed. However, the modified equation two assumes that vegetation cover increases the critical wind speed without changing the surface wind speed. The latter approach aligns with Lyles and Allison's [36,37] or Marshall's [38] approach. In practical applications, vegetation cover may affect both surface and critical wind speeds. Wasson's assessment approach encounters the challenge of selecting between these two equations. In contrast, Huang et al. applied Fryberger's method [33] to propose the sand-transport factor combined with  $DP$  to evaluate sand transport in complex environments [35]. This approach yielded favorable outcomes in practical applications. However, the sand-transport factor derives from extensive field observation data, limiting the method's generalizability. In conclusion, there is currently a paucity of unified and effective assessment models for sand transport that accurately evaluate the impacts of vegetation degradation on flat surfaces.

This study conducted field observations along the Oshang Railway to analyze the aeolian sand transport conditions in the region with the aim of guiding the implementation of wind and sand protection measures along this railway line. Additionally, inspired by Fryberger's framework [33], an empirical expression was proposed to assess sand transport on flat surfaces affected by vegetation cover, thereby enriching the field of aeolian physics research. Furthermore, the study investigated threshold conditions for the significant impact of vegetation cover on sediment transport rates, providing insights on sparse afforestation strategies to mitigate wind-sand erosion in the area.

## 2. Methods

### 2.1. Observation Positions and Instruments

The railway extends over 116 km, stretching from Aogaoturi Station in Otog Front Banner to Shanghai-Temple West Station in the western direction (see Figure 2a). Five observation sites were strategically chosen along the railway to account for variations in surface herbaceous vegetation cover across different regions, as detailed by Casado et al. [39]. In our selection process of observation positions, we not only considered variations in fractional vegetation cover but also factored in the angles between the main wind direction of sand transport and the railway (spanning from acute to right angles). This approach aims to enhance the accuracy of wind and sand monitoring results, ensuring they more faithfully depict the genuine sand-transport characteristics around the railway. Ultimately, this guides the effective execution of sand-control projects for the railway. These locations are visually depicted in Figure 2. The terrain surrounding the observation sites predominantly features flat topography, characterized by sandy surfaces and herbaceous vegetation.

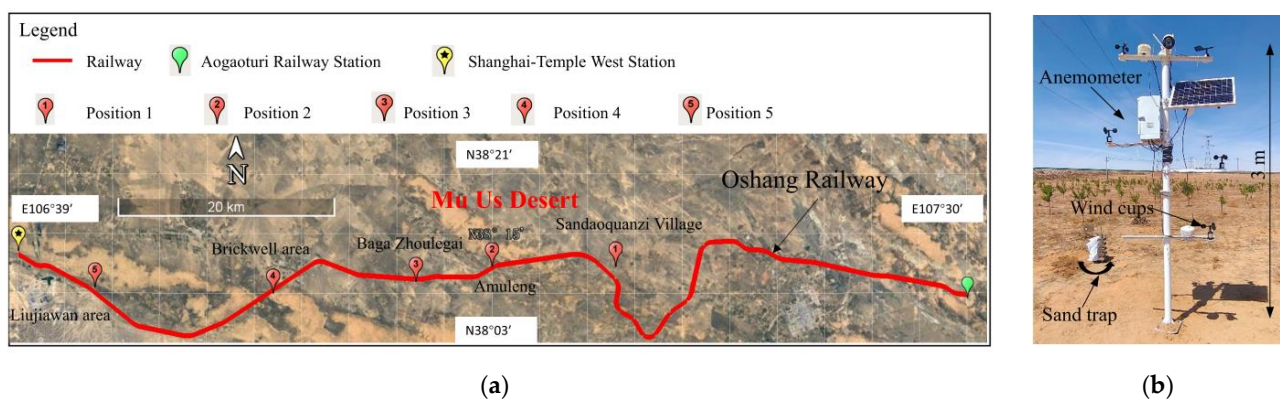


**Figure 2.** Observation positions (a) and instruments arrangement (b).

The observation instruments used in each observation position are an anemometer and a rotating sand collector, as shown in Figure 2b. The anemometer has an overall height of 3 m, with wind cups at heights of 1 m, 1.5 m, 2 m and 3 m, with a sampling frequency of 1/180 Hz. The rotating sand collector monitors the cumulative amount of sand transported by blowing wind at different directions and heights and can be rotated 360° with the direction of the wind. The sand collector is 50 cm tall and comprises five layers of sand inlet channels, each with double sand inlets. The first layer of the sand trap is positioned 2.5 cm above the ground, and the vertical distance between the two channels is 6.25 cm. The sand trap has geometric dimensions of 5 × 5 cm (length × width), and each sand inlet is accompanied by a bag with a sand capacity of 4 kg. The experimental observation period lasted five months, from March to June 2023.

### 2.2. Data Processing and Hypotheses

The DP (Drift Potential) [33] is utilized to assess the sand-transport potential along the railway:

$$DP = v^2(v - v_{*t}) \cdot f \quad (1)$$

where the DP is the drift potential (VU),  $v$  is the average wind speed at a height of 10 m (knot, 1 knot = 0.514444 m/s),  $v_{*t}$  is the threshold speed (knot), and  $f$  is the sand-moving wind frequency, expressed as a percentage (%).

The RDP is derived from the synthesis of drift potential vectors, reflecting the net drift potential. Additionally, RDD represents the direction of synthetic sand transport, indicating the net direction of sand transport potential. Fryberger categorized the wind energy environment into three levels: the low wind energy environment ( $DP < 200$  VU), the medium wind energy environment ( $200 \text{ VU} < DP < 400 \text{ VU}$ ), and the high wind energy environment ( $DP > 400 \text{ VU}$ ) [33].  $RDP/DP$  serves as the wind direction variability index,

with smaller values indicating greater wind direction changes, and vice versa. When the value is less than 0.3, it signifies low wind variability, 0.3–0.8 indicates medium wind variability, and above 0.8 suggests high wind variability [33].

To study the assessment of sand transport under the influence of fractional vegetation cover, we propose the following hypotheses:

**Hypothesis 1.** *Following the Fryberger’s framework [33], the sand transport rate is assumed to be proportional to drift potential. Thus, we posit that vegetation impacts drift potential, consequently influencing the sand transport rate.*

**Hypothesis 2.** *The precise computation of threshold wind speed under the influence of fractional vegetation cover holds paramount importance in evaluating drift potential. In their recent study, Sun offers an empirical formula for the impact threshold wind speed in the absence of rebound, derived from meticulous numerical simulations of randomly dispersed, discontinuous crusts [40]. This situation parallels wind-sand movement under sparse grass cover, thus, we posit that employing this formula to assess initiation wind speed under fractional vegetation cover influence yields relatively accurate results.*

**Hypothesis 3.** *The area is characterized by grass vegetation. Building on Wasson et al.’s research [36], we solely focus on fractional vegetation cover (FVC), disregarding the effects of plant height and porosity.*

The threshold wind speed ( $v_{*t}$ , the minimum wind speed to maintain wind-blown sand) was calculated:

$$v_{*t} = 5.75u_{*t}\lg\left(\frac{z}{z_0}\right) \quad (2)$$

where  $u_{*t}$  is the impact threshold wind speed;  $z$  is the height (m), taking 10 m;  $z_0$  is the aerodynamic roughness (m).

According to hypothesis 2: the impact threshold wind speed ( $u_{*t}$ , the minimum wind speed to maintain wind-blown sand) of 250  $\mu\text{m}$  sand particles was calculated according to Sun’s formula [40]:

$$u_{*t} = 0.066 \cdot e^{\frac{FVC}{0.379}} + 0.13 \quad (3)$$

where  $FVC$  is the average fractional cover of crust or grass vegetation (%).

Drawing from Bagnold’s research findings [41], we ascertain that the initiation wind speed correlates with the square root of the particle size. To refine our understanding, we will extrapolate this equation for further correction.

$$u_{*t} = \sqrt{d/D} \left( 0.066 \cdot e^{\frac{FVC}{0.379}} + 0.13 \right) \quad (4)$$

where  $d$  is the mean particle size ( $\mu\text{m}$ );  $D$  is the reference particle size (250  $\mu\text{m}$ ).

Particle size analysis is conducted on the sand source within the experimental area, and the following formula is applied to obtain the median particle size and distribution through fitting [40]:

$$y = A \exp\left(-0.5\left(\frac{x-d}{B}\right)^2\right) \quad (5)$$

where  $A$  and  $B$  are the fitting parameters;  $d$  is the mean particle size ( $\mu\text{m}$ ).

The average aerodynamic roughness  $z_0$  at the observation location is obtained by [42]:

$$\lg(z_0) = \frac{\lg z_2 - t \lg z_1}{1 - t} \quad (6)$$

where  $t = v_2/v_1$ ,  $v_2$  and  $v_1$  are the average wind speed at the reference height  $z_2$  and  $z_1$  (m/s), respectively.



The 10 m height average wind speed at the observation location is extrapolated by the logarithmic wind speed profile equation [42]:

$$\frac{v}{v_*} = \frac{1}{K} \ln\left(\frac{z}{z_0}\right) \quad (7)$$

where  $K$  is Von Kármán constant,  $v_z$  is the wind speed at the reference height  $z$  (m/s), and  $v_*$  is the friction wind speed (m/s).

In vertical space, the cumulative sand transport flux in all wind directions is fitted using a negative exponential function [12]:

$$f_z = a \cdot \exp(-z/b) + c \quad (8)$$

where  $f_z$  is the cumulative sand transport flux in each direction at  $z$  height ( $\text{kg}/(\text{m}^2 \cdot \text{a})$ ) and  $a$ ,  $b$  and  $c$  are the fitting parameters.

The cumulative unit-width sand transport rate for all wind directions can be expressed as follows:

$$F = \int f_z dz \quad (9)$$

The unit-width sand transport rate  $Q_i$  for each wind direction  $i$  can then be expressed as follows:

$$Q_i = \frac{F \times DP_i}{\sum_{i=1}^{16} DP_i} \quad (10)$$

where  $Q_i$  is the unit-width sand transport rate in wind direction  $i$  ( $\text{kg}/(\text{m} \cdot \text{a})$ );  $F$  is the cumulative sand transport rate in all wind directions ( $\text{kg}/(\text{m} \cdot \text{a})$ );  $DP_i$  is the drift potential in direction  $i$  (VU);  $RQ$  is the vector synthesis of  $Q_s$  which represents the net sand transport rate, and the direction of  $RQ$  is the net sand-transport direction.

### 3. Results

#### 3.1. Wind Field and Sand Source

The intensity of the wind field dictates the potential for sand transport. Initially, we gathered data on the raw monitored wind speeds, and proceeded to generate wind rose diagrams and determine sand-moving wind frequencies [25], and ultimately we computed the drift potential.

Figure 3 depicts wind speed rises that are plotted at 2.5 m/s intervals at all observation positions. The wind speeds at locations 1, 2, and 5, which belong to the strong-wind zone, are graded 2–3 levels higher than the wind speeds at locations 3 and 4, which belong to the weak-wind zone.

At position 5, the wind speed is divided into six gradients with the maximum wind speed ranging from 12.5 to 15 m/s and the main wind direction being east. The wind speed of 0–2.5 m/s accounts for 56.8% of the total wind speed, and the proportion of calms is 1.8%. At position 4, the wind speed is divided into four gradients with the maximum wind speed range being 7.5–10 m/s, and the main wind direction being west. The wind speed range of 0–2.5 m/s is as high as 66.6%, and the proportion of calms is 2.88%. At position 3, the wind speed is divided into four gradients. The maximum wind speed range is 7.5–10 m/s, with the main wind direction being W and SW. The wind speed range of 2.5–5 m/s accounts for as much as 50.4%, and the proportion of calms is 0.79%. At position 2, the wind speeds are divided into six gradients, with maximum speeds ranging from 12.5 to 15 m/s. The primary wind directions are S, SW, and W. The proportion of wind speeds between 0 and 2.5 m/s accounts for 61.8% of the total wind speeds, while the proportion of calms is 6.1%. At position 1, the wind speed was divided into seven gradients, with the maximum wind speed ranging from 15 to 17.5 m/s and the main wind direction being NE and S. The proportion of wind speeds between 2.5 and 5 m/s accounted for 43.9% of the total wind speed, while the proportion of calms was 0.34%.

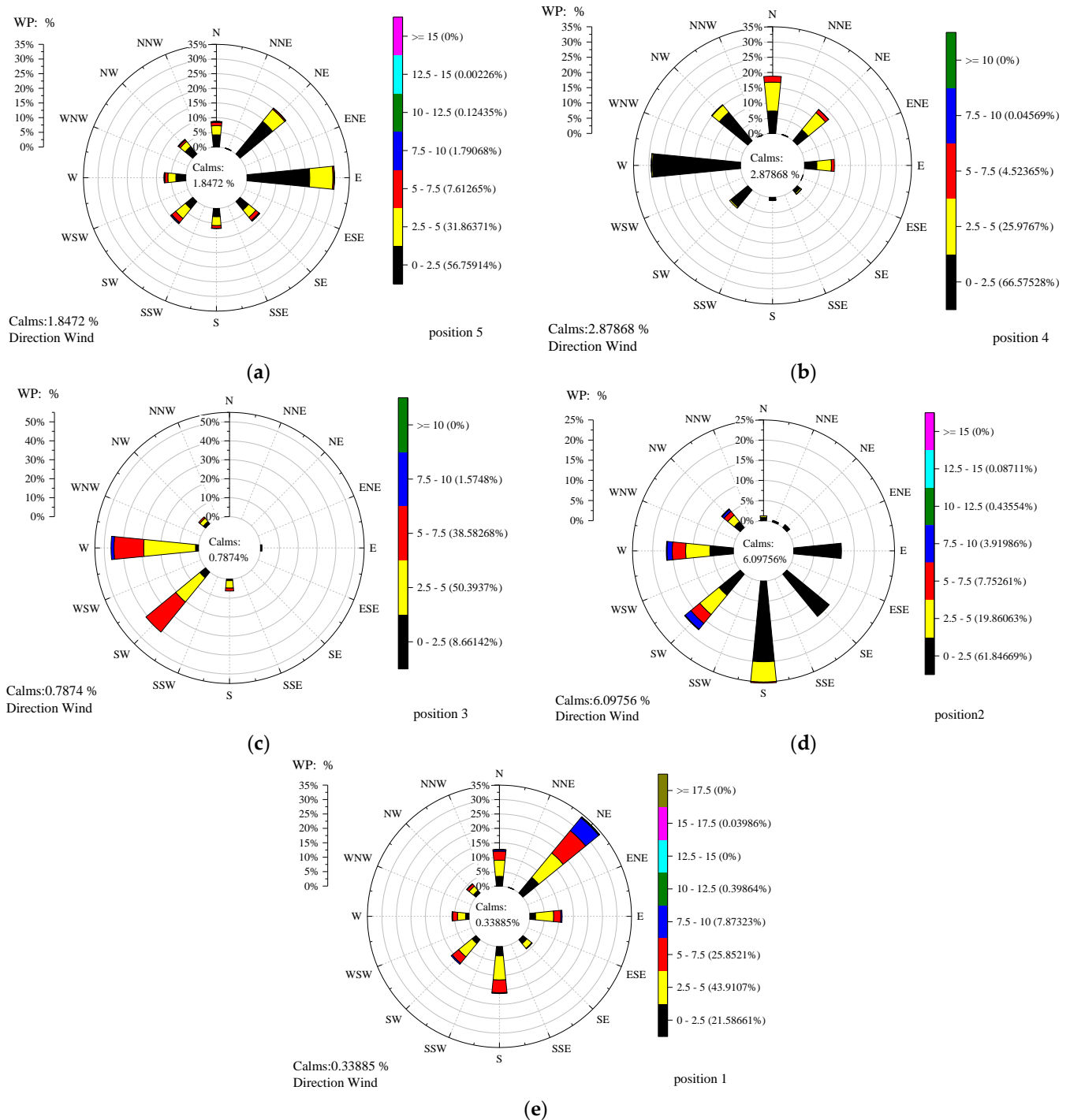


**Figure 3.** Wind Roses (af 3 m height) in at different monitoring positions (5–1), (a–e) represent position 5 to 1, respectively.

The sand-moving wind frequency [25] varied significantly (see Figure 4) among the observation positions, with the high frequency at location 3 (90.55%) and the low frequency at the remaining locations. At location 5, the total sand-moving wind frequency was 41.39%, with the main wind directions for sand movement being N, NE, E, SE, S, SW, W, and NW, with values of 4.52%, 5.8%, 8.4%, 4.9%, 4.1%, 6.4%, 4.0%, and 3.1%, respectively. The sand-moving wind frequency at location 4 is 30.54%. The main values of sand-moving wind frequency are 11.4%, 8.5%, and 5.7% for N, NE, and E directions, respectively. At the location 3, the total sand transport wind frequency is 90.55%. The main directions for sand-moving wind frequency are S, SW, and W, with values of 5.5%, 37.0%, and 44.9%,

respectively. Location 2 has a total sand transport wind frequency of 32.05%. The main directions for sand-transport wind are S, SW, W, and NW, with values of 5.3%, 11.1%, 10.8%, and 4.1%, respectively. Location 1 has a total sand transport wind frequency of 34.16%. The main directions for sand transport wind are N, NE, E, S, SW, and W, with values of 3.6%, 16.24%, 2.9%, 4.7%, 3.3%, and 1.9%, respectively.

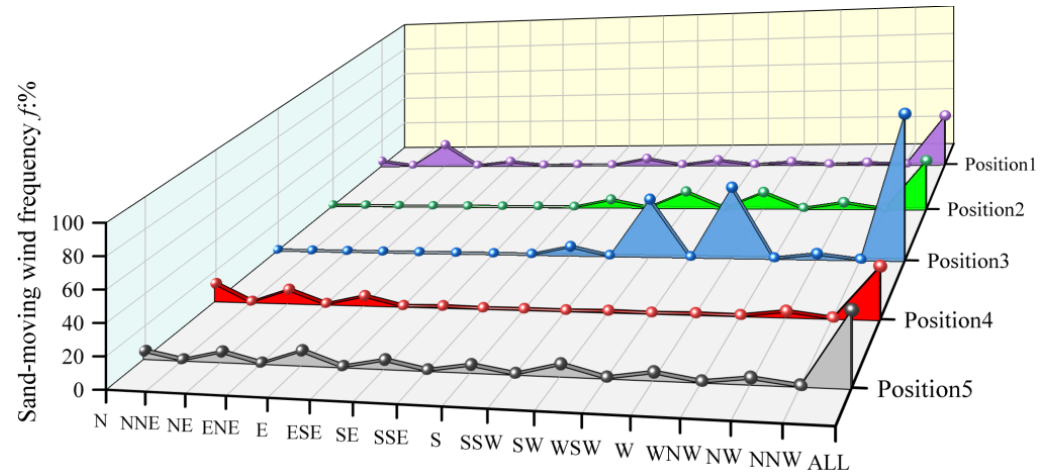


**Figure 4.** The sand-moving frequency at different monitoring positions (5–1).

Sand samples were collected from various monitoring positions and subjected to particle size analysis the results of which are displayed in Figure 5. These results were analyzed using Equation (5) to attain the median particle sizes. At location 5, the fitting parameters of Equation (5) A and B are 31.4 and 53.4, respectively, resulting in a median particle size ( $d$ ) of 257  $\mu\text{m}$  and a coefficient of determination ( $R^2$ ) of 0.99. At location 4, the parameters A and B are 22.1 and 57.9, leading to a median particle size of 200  $\mu\text{m}$  and an  $R^2$  of 0.96. At location 3, A and B are set at 15.9 and 51.7, resulting in a median particle size of 142.5  $\mu\text{m}$  and an  $R^2$  of 0.95. At location 2, with parameters A and B of 42.8 and 39.3, the median particle size is 274  $\mu\text{m}$  and the  $R^2$  is 0.97. Lastly, at location 1, the parameters A and B are 24.9 and 66.6, resulting in a median particle size of 271  $\mu\text{m}$  and an  $R^2$  of 0.96.

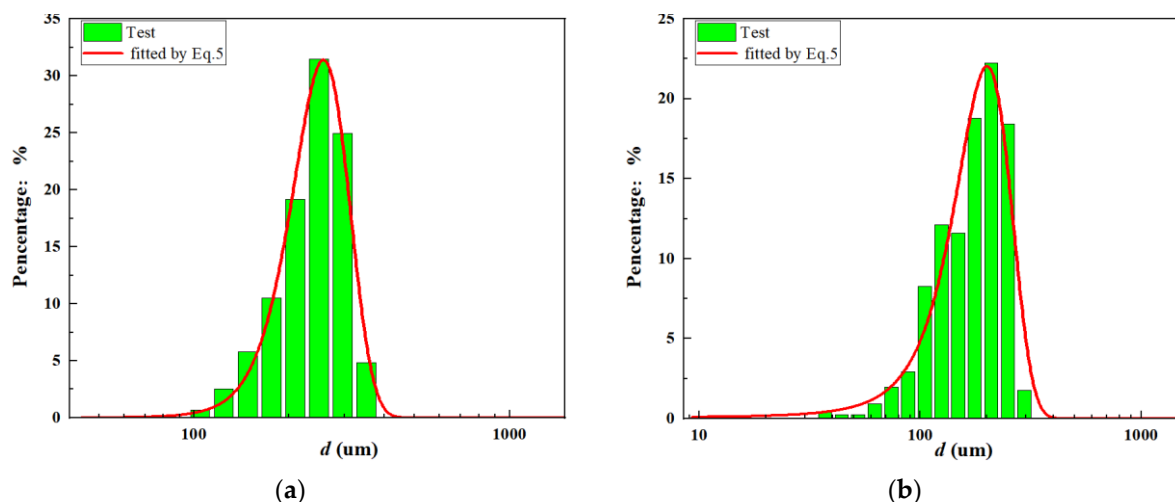


**Figure 5.** Cont.

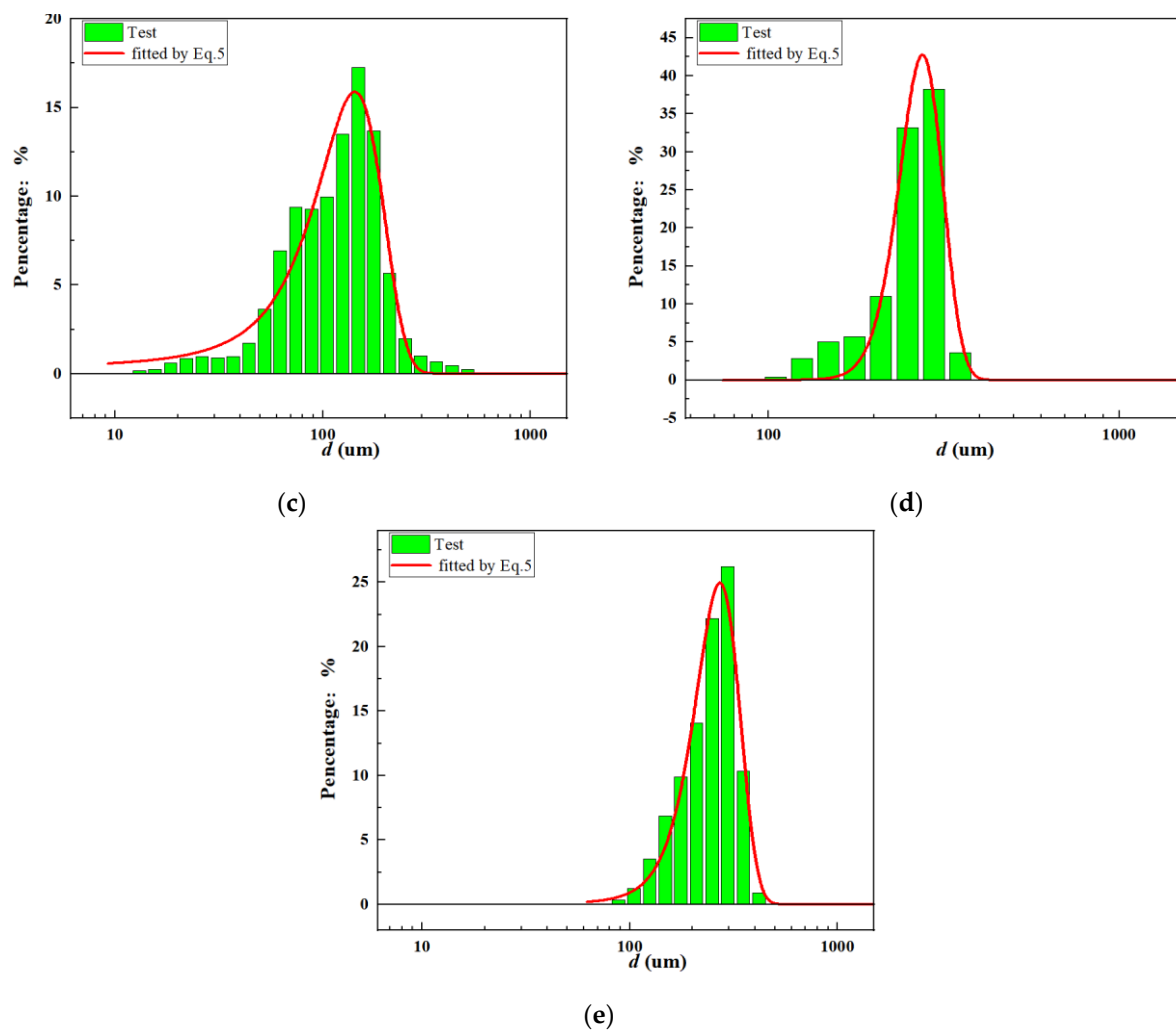


**Figure 5.** Particle size distribution monitoring positions (5–1), (a–e) represent position 5 to 1, respectively.

We used Equation (6) to determine the mean aerodynamic roughness and fitted the mean wind speeds at different heights (1 m, 1.5 m, 2 m and 3 m) to extrapolate the wind speeds at the 3 m height to the wind speed at the 10 m height (by Equation (7)). Next, we calculated the threshold speed  $v_{*t}$  and impact threshold wind speed  $u_{*t}$  (see Table 1) for the region (Equations (2) and (4)) by combining the results of the grain size (refer to Figure 5). The particle size of the sand source and fractional vegetation cover determine the threshold wind speed. The greater the fractional vegetation cover and sand source particle size, the higher the threshold wind speed.

**Table 1.** The threshold speed  $v_{*t}$  and impact threshold wind speed  $u_{*t}$ .

Position	$u_{*t}$ (m/s)	Threshold Speed at 10 m Height $v_{*t}$ (knots)
5	0.28	9.9
4	0.21	6.9
3	0.22	6.2
2	0.24	8.6
1	0.38	13.5

The determination of the  $DPs$  at each observation position (refer to Figure 6) was performed by utilizing the threshold wind speed along with the extrapolated wind speed at a 10 m height, as derived from Equation (1) [33]. Observation positions 2–3 are situated



in high wind energy environments, while position 4 experiences low wind energy, and positions 5 and 1 reside in a medium wind energy setting. Synthesized sand plumes at positions 5, 3, and 2 exhibit directions between W and WSW, whereas those at positions 4 and 1 align between NE and NNE (refer to Figure 5). The  $RDP/DP$  values for positions 5–1 are 0.22, 0.72, 0.88, 0.77, and 0.6, respectively. Notably, the wind direction at position 5 exhibits significant variability. At position 3, the sand-moving wind direction remains nearly constant, primarily west-southwesterly. For the remaining observation positions, the sand-moving wind-direction index ranges from low to medium levels [33].

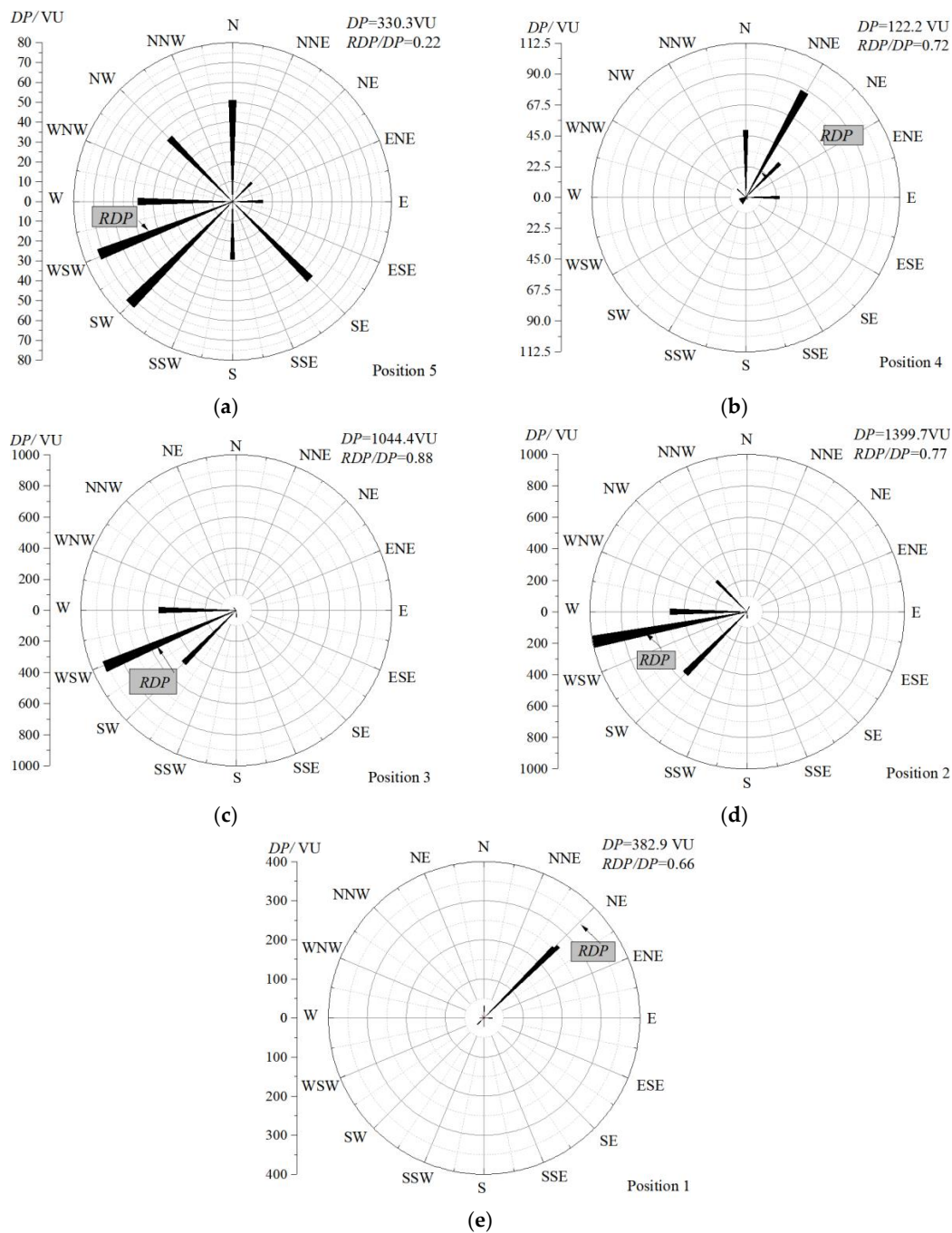


**Figure 6.** The DPs at different monitoring positions, (a–e) represent position 5 to 1, respectively.

### 3.2. Surface Fractional Vegetation Cover

The experimental site features a predominantly flat terrain. Anthropogenic activities, highlighted by Wang et al. [4], have substantially degraded the grassland. Figure 7

illustrates significant variations in *FVC* [39] among observation positions. During the monitoring period, the average fractional vegetation cover at positions 1–5 is 51.6%, 20.3%, 13.2%, 11.1%, and 33.3%, respectively. Positions 1 and 5 fall into the category of medium fractional vegetation cover, while position 2 is characterized by low fractional vegetation cover. Due to pronounced surface degradation, positions 3 and 4 are designated as having ultra-low fractional vegetation cover.

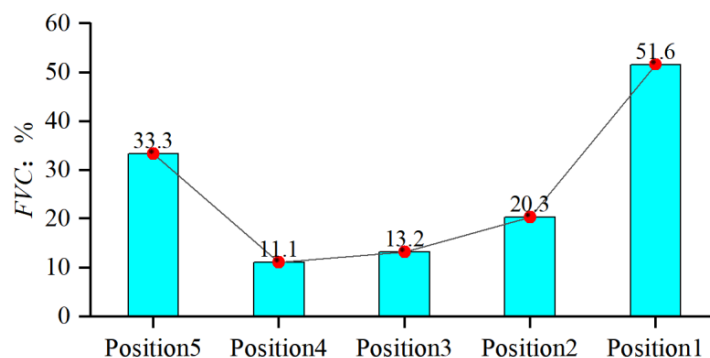


**Figure 7.** The fractional vegetation covers at different monitoring positions (5–1).

### 3.3. Sand Transport Characteristics

Figure 8 illustrates the cumulative sand fluxes in all wind directions at different observation positions. The sand fluxes exhibit negative exponential changes with height (Equation (8)), which aligns with the monitoring findings of Wang et al. [12]. The coefficients of determination ( $R^2$ ) of the fitted regression equations are all higher than 0.98. As shown in Figure 9, the cumulative unit-width sand transport rates were calculated using the cumulative sand fluxes in all wind directions (by Equation (9)). At the observation positions 5–1, the cumulative unit-width sand rates were 5.40 kg/(m·a), 303.70 kg/(m·a), 228.60 kg/(m·a), 102.90 kg/(m·a), and 5.80 kg/(m·a) for all wind directions 1–5, respectively (see Figure 9). The strongest sand transport is observed at positions 4, 3, and 2, which is significantly higher than that at positions 5 and 1.

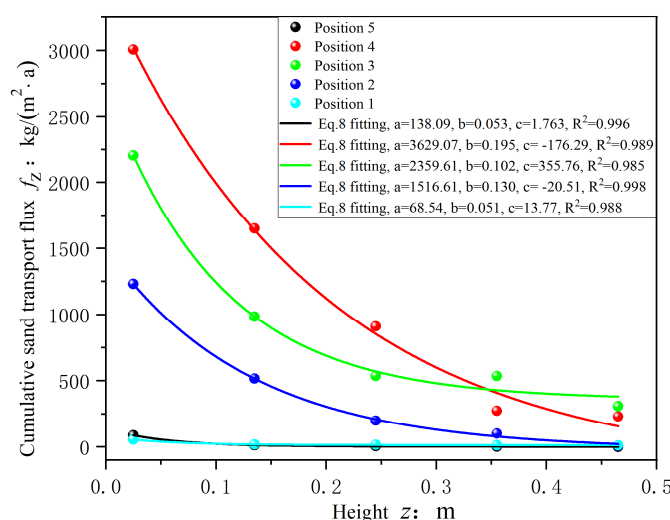


**Figure 8.** The cumulative fluxes of sand transport of all wind directions at different positions (5–1).

Figure 10 presents the average unit-width sand transport rate (calculated by Equation (10)) for each wind direction at each observation position. Observation positions 5–1 had an annual average maximum net sand-transport rate of 1.20 kg/(m·a), 218.00 kg/(m·a), 201.00 kg/(m·a), 80.00 kg/(m·a), and 3.70 kg/(m·a), respectively. The main sand transport direction at observation positions 5, 3, and 2 was between WSW and W, while the main sand transport direction at observation positions 4 and 1 was between NNE and NE.

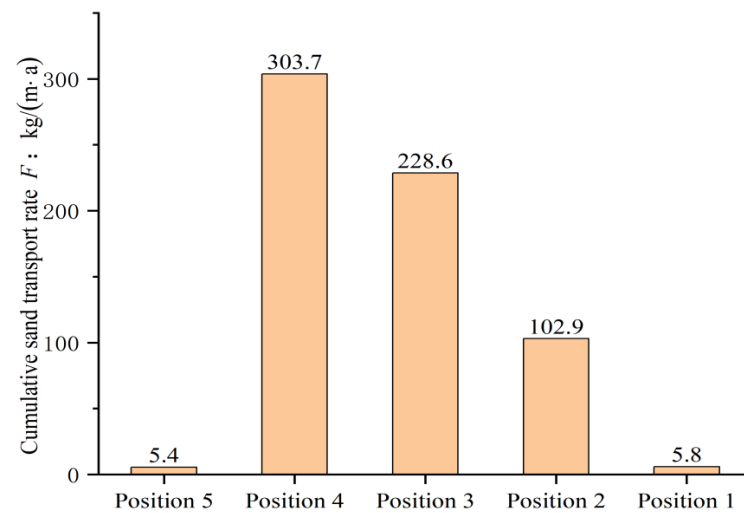


Figure 9. The cumulative sand transport rate of all wind directions at different positions(5–1).

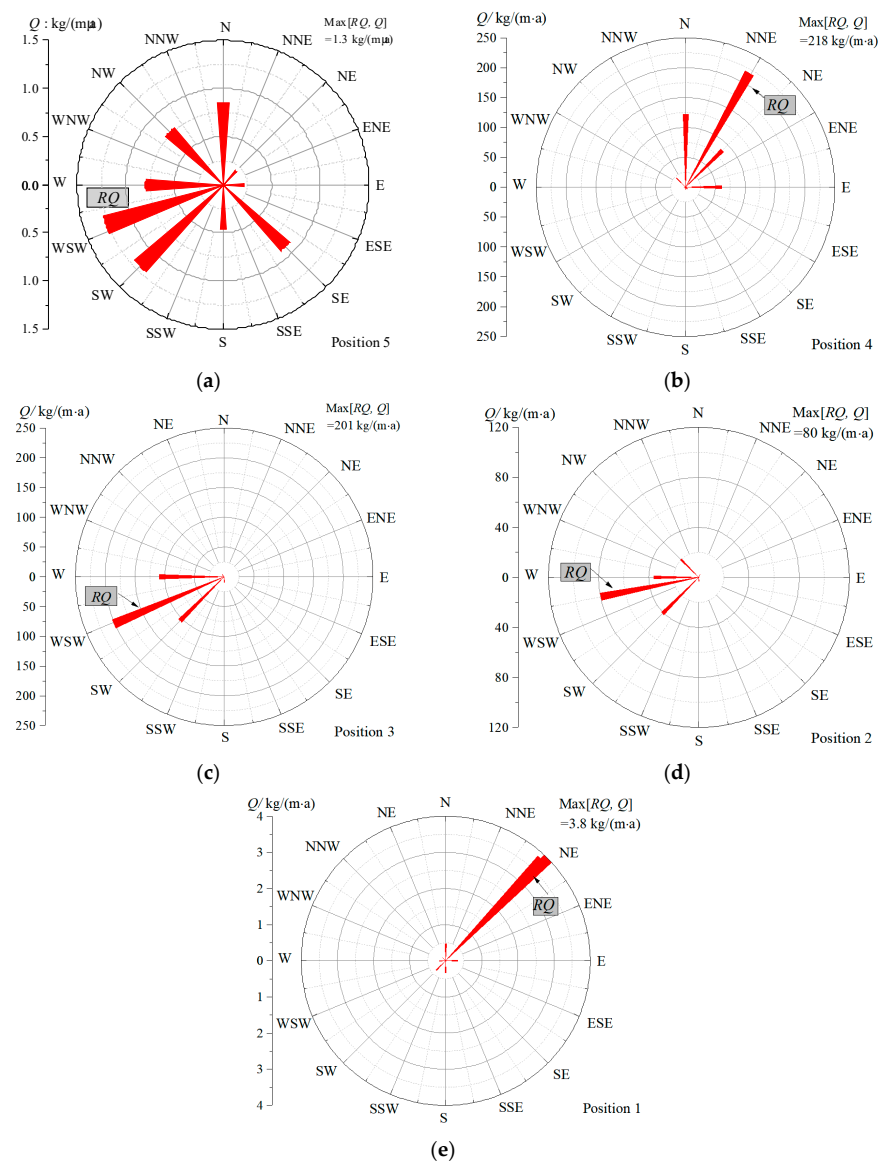


Figure 10. The  $Q$ s at different monitoring positions, (a–e) represent position 5 to 1, respectively.

Comparing Figures 6 and 10, the direction of synthesized drift potential ( $RDD$ ) dictates the net sediment transport direction. As illustrated in Figure 6, the  $DP$  values at location 5-1 are 330.3 VU, 122.2 VU, 1044.4 VU, 1399.7 VU, and 382.9 VU, respectively. Figure 10 reveals that the net sand transport rates at the same location are 1.2 kg/(m·a), 218 kg/(m·a), 201 kg/(m·a), 80 kg/(m·a), and 3.8 kg/(m·a). Contrary to Fryberger's viewpoint [33], the magnitude of  $DP$  does not perfectly align with the sediment transport rate. This discrepancy arises because the  $DP$  accurately characterizes the sand transport traits of loose and flat surfaces [33,34]. However, vegetation coverage and sand particle size introduce significant disparities between the sand transport rate and drift potential [35,36,43]. This is evident in locations with minimal vegetation coverage experiencing heightened sand transport (e.g., locations 4 and 3), while areas with dense vegetation coverage exhibit pronounced suppression of wind and sand flow (e.g., locations 5 and 1).

#### 4. Discussion

##### 4.1. Spatial Characteristics of Aeolian Sand Transport along the Oshang Railway

Referring to the monitoring findings mentioned earlier, we have pinpointed the transport rate characteristics along the Oshang Railway by the orthogonal decomposition, offering valuable insights to inform the implementation of on-site measures for wind and sand protection.

Figure 11 illustrates the sand transport characteristics along the railway. At observation position 5 in the Liujiawan area, the net synthetic unit-width sand transport rate is 1.20 kg/(m·a), with components of 0.93 kg/(m·a) perpendicular to the railroad and 0.76 kg/(m·a) parallel to it. The angle between the railroad and its direction is  $51^\circ$ . At observation position 4 in the Brickwell area, the net synthetic unit-width sand transport rate is 218.0 kg/(m·a). The angle between the railroad and its direction is  $24^\circ$ , with components perpendicular and parallel to the railroad being 199.1 kg/(m·a) and 88.7 kg/(m·a), respectively. At observation position 3 in the Baga Zhoulegai area, the net synthetic unit-width sand transport rate is 201.0 kg/(m·a). The angle between the railroad and its direction is  $21^\circ$ , with components perpendicular and parallel to the railroad being 72.1 kg/(m·a) and 187.6 kg/(m·a), respectively. At observation position 2 in Amuleng, the net synthetic unit-width sand transport rate was 79.7 kg/(m·a). The angle between the railway and its direction was  $19^\circ$ , with sand transport rates of 75.36 kg/(m·a) perpendicular to the railway and 25.95 kg/(m·a) parallel to it. Observation position 1 in Sandaoquanzi Village has a net synthetic unit-width sand transport rate of 3.80 kg/(m·a). The angle between the railroad and its direction was  $86^\circ$ , and the sand transport rate perpendicular to the railroad direction was 3.78 kg/(m·a).

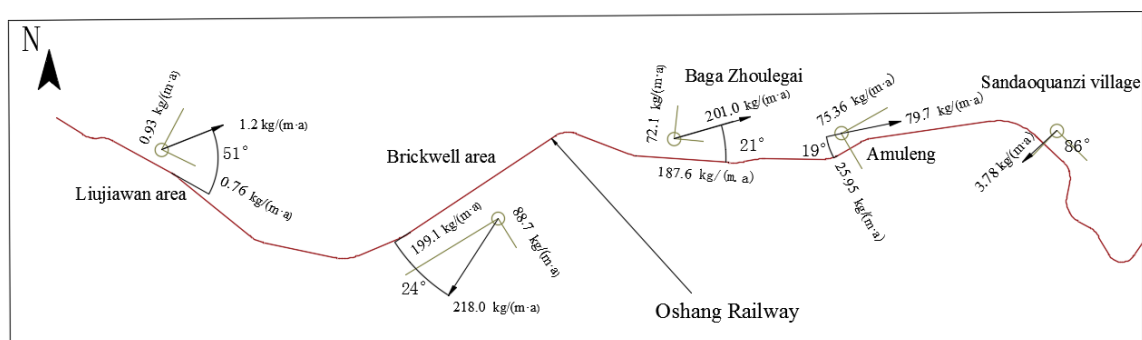


**Figure 11.** The sand transport characteristics along the railway.

Drawing from the aforementioned observed characteristics, we have delineated the sediment transport distribution pattern along the Oshang Railway: the intensity of sand transport along the Oshang Railway decreases successively in the Brickwell, Baga Zhoulegai, Amuleng, Sandaoquanzi Village, and Liujiawan areas (see Figure 10). Perpendicular to the railway's direction, the sand transport intensity in typical areas follows this order:

Brickwell area > Baga Zhouluegai area > Amureng > Sandaoquanzi Village > Liujiawan. Similarly, parallel to the railroad, the sand-transport intensity sequence is as follows: Brickwell area > Baga Zhouluegai area > Amureng > Liujiawan > Sandaoquanzi Village.

Our monitoring results reveal that in the intense blown sand transport regions (locations 4, 3, and 2), the primary sand transport direction forms acute angles with the Oshang Railway, measuring  $24^\circ$ ,  $21^\circ$ , and  $19^\circ$ , respectively. This observation is consistent with the guiding principles for railway alignment in such environments, emphasizing alignment parallel to the prevailing wind direction to mitigate sand deposition and wind erosion [44]. When implementing sand control measures along the railway, it is crucial to consider both perpendicular and parallel wind-sand transport directions relative to the railway. Hence, we recommend deploying zig-zag-shaped sand barriers [18] to shield against sand movement at locations 4, 3, and 2.

#### 4.2. Factors Affecting Sand Transport

Table 2 displays statistical findings regarding *DP* information, surface fractional vegetation cover (*FVC*), and sand transport rate (*Q*) at observation points along the Oshang Railway.

**Table 2.** Statistics on drift potential, net unit-width sand transport rate and surface properties at each monitoring position along the Oshang Railway.

Position	<i>DP</i> (VU)	<i>RDP/DP</i>	Unit-Width Net Sand Transport Rate <i>Q</i> (kg/(m·a))	Angle between the RQ and the Railway ( $^\circ$ )	Surface <i>FVC</i> (%)
5	330.3 (medium)	0.22	1.2	51	Medium turf (33.3%)
4	122.2 (low)	0.72	218	24	Sandy surface (11.1%)
3	1044.4 (high)	0.88	201	21	Sandy surface (13.2%)
2	1399.4 (high)	0.77	80	19	sparse turf (20.3%)
1	563.4 (high)	0.66	3.8	86	Hard turf (50.6%)

The results reveal that dense grass cover significantly impedes blown sand transport, irrespective of the wind energy environment (Observation Position 1) or (Observation Position 5), resulting in negligible blown sand flux. Observation data at Position 4 indicate persistent blown-sand activity on sandy surfaces with severe surface degradation, despite their low wind energy environments. Moreover, Observation data at Position 3 illustrate that when grasslands reach the critical state of surface sanding, high sand transport occurs due to the interplay between the high wind environment and surface characteristics. Conversely, for sparse turf surfaces at Observation Position 2, sand transport activity remains moderate despite the high wind energy environment. These results further affirm that sparse vegetation (with fractional vegetation coverage of 15–25%) effectively mitigates wind-drift sand flow [45]. Blown sand transport is primarily governed by surface properties [21] and wind field characteristics, aligning with the findings of Huang et al. [35].

Based on the findings of previous studies [33,34], it is established that the sediment transport rate is directly proportional to the sediment transport potential ( $Q \propto DP$ ). To delve deeper into the relationship between fractional vegetation cover and these variables, we employed correlation analysis techniques [46–48] to assess the correlation between the sand transport rate-to-drift potential ratio and fractional vegetation cover. The results are summarized in Table 3. Notably, there exists a strong negative correlation between the sand transport rate to drift-potential ratio ( $R = Q \cdot f / DP$ ) and fractional vegetation cover, as evidenced by the Pearson correlation, Kendall correlation, and Spearman correlation coefficients of  $-0.54$ ,  $-0.80$ , and  $-0.90$ , respectively.

**Table 3.** Correlation analysis of the ratio of *Q* to *DP* with the *FVC*.

Correlation Analysis		<i>FVC</i>
The ratio of <i>Q</i> to <i>DP</i> , $R = Q \cdot f / DP$	Pearson correlation	$-0.54$
	Kendall Correlation	$-0.80$
	Spearman Correlation	$-0.90^*$

Note: \* represents significant correlation.



#### 4.3. Characterisation of Sand Transport under the Influence of Vegetation

The factors influencing sand transport are numerous, including wind conditions [41, 49,50], sand particle size [41,49,50], sand moisture content [51], and fractional vegetation cover [43,52]. Along the railway line, the minimal rainfall but significant evaporation means we disregard the influence of sand source and moisture content on sediment transport. Instead, fractional vegetation cover and drift potential become the primary factors affecting sand transport in the area (see Section 4.2). We will delve into the functional relationship between sand transport rate  $Q$ , drift potential ( $DP$ ),  $f$  is the sand-moving wind frequency and fractional vegetation cover ( $FVC$ ).

To facilitate comparison with Wasson's results, we have normalized the above variables. The dimensionless ratio of the sand transport rate ( $Q$ ) and the sand-moving wind frequency  $f$  to drift potential ( $DP$ ) is regarded as a function (refer to Equation (11)) of the alteration in normalized fractional vegetation cover, illustrated as follows:

$$\left[ \frac{Q \cdot g \cdot f}{0.136 \times DP \cdot \rho_a} \right]_{\text{Normalized}} = e \times \exp(-[FVC]_{\text{Normalized}}/p) + r \quad (11)$$

where  $Q$  is the unit-width sand transport rate ( $\text{kg}/(\text{m} \cdot \text{s})$ );  $g$  is the gravitational acceleration ( $9.81 \text{ m/s}^2$ );  $DP$  is the drift potential (VU);  $\rho_a$  is the air density ( $1.290 \text{ kg/m}^3$ );  $FVC$  is the fractional vegetation cover;  $f$  is the sand-moving wind frequency;  $e$ ,  $p$  and  $r$  are fitting parameters.

The presence of fractional vegetation cover on flat surfaces emerges as a pivotal factor mitigating drift potential, thereby influencing the actual sand transport rate. In Figure 12, the dimensionless ratio  $Q \cdot g \cdot f / (0.136 \times DP \cdot \rho_a)$ , representing the sand transport rate ( $Q$ ) and  $DP$ , exhibits a negative exponential trend correlating with increasing normalized  $FVC$  in this locale, aligning with Wasson's study results [36]. Table 4 presents the empirical parameters ( $e$ ,  $p$ ,  $r$ ) and the coefficient of determination ( $R^2$ ). Blown-sand activity diminishes when  $FVC$  equals or exceeds 20.3%.

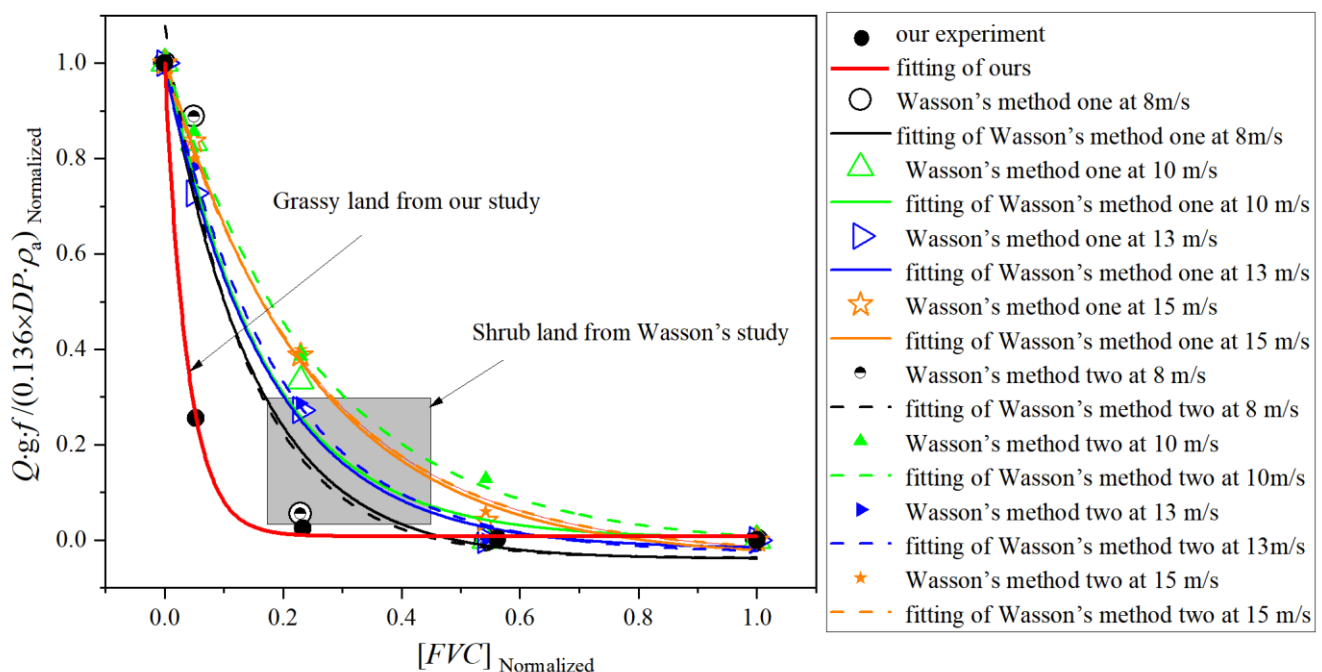


**Figure 12.** Normalized relationship between the dimensionless ratio of sand charge ( $Q$ ) and drift potential ( $DP$ ) and fractional vegetation cover ( $FVC$ ).

**Table 4.** Statistics on parameters of fitting Equations (Equation (11)).

Type	e	p	r	R <sup>2</sup>	Condition
Q from observation data, Ours	0.992	0.038	0.0079	0.99	this paper
	1.058	0.15	−0.04	0.908	8 m/s
Q Calculated from Wasson’s method one, 1986 [36]	1.019	0.166	0.0034	0.97	10 m/s
Q = B × (V <sub>0</sub> · f(FVC) − V <sub>t</sub> ) <sup>3</sup>	1.010	0.174	−0.018	0.996	13 m/s
	1.053	0.2456	−0.039	0.994	15 m/s
	1.12	0.138	−0.038	0.916	8 m/s
Q Calculated from Wasson’s method two, 1986 [36]	1.02	0.256	−0.0133	0.996	10 m/s
Q = B × (V <sub>0</sub> − V <sub>t</sub> · g(FVC)) <sup>3</sup>	1.03	0.189	−0.028	0.996	13 m/s
	1.027	0.251	−0.032	0.996	15 m/s

Note: V<sub>0</sub> is incoming velocity, V<sub>t</sub> is threshold wind speed, f(FVC) and g(FVC) are the influencing functions of vegetation cover FVC on V<sub>0</sub> and V<sub>t</sub>, respectively.

According to Buckley’s findings [53], it holds for  $FVC > 17\%$  and implies any given V at which Q falls to 0. Our results indicate that with vegetation cover below 20.3%, sand transport experiences exponential growth as vegetation degrades. This value surpasses Buckley’s findings [53] yet falls below Wasson’s [36]. The variance between Wasson’s and Buckley’s findings [36,53] and our study may stem from the diverse impacts of herbaceous plants and shrubs on blowing sand, as well as differences in plant geometry and layout [53]. While our study does not attempt to incorporate these factors into its equation, it still provides valuable insights for guiding sand-control initiatives along the regional railway and assessing blown sand movement on flat surfaces influenced by vegetation. Therefore, we formulated an empirical equation for the sediment transport rate tailored to this region under the influence of vegetation coverage:

$$Q = C_{(FVC)} \cdot \frac{\rho_a}{g} V^2 (V - V_{*t}) \quad (12)$$

This formula enhances Lettau’s sand transport rate equation [54] in two key aspects ( $Q = \frac{C \rho_a}{g} V^2 (V - V_{*t})$ , where  $C_{(FVC)}$  is a parameter representing surface properties), enabling it to effectively depict sand transport rates during grassland degradation. Our improvements include: firstly, integrating the empirical formula proposed by Sun [40] for more accurate calculations of  $V_{*t}$ , as described in Equations (2) and (4), which considers the impact of vegetation coverage, particle size of sand source, and surface roughness. Secondly, we introduced a dimensionless function  $C_{(FVC)}$  controlled by fractional vegetation cover (FVC) to adjust the Lettau formula:

$$C_{(FVC)} = C_0 \times \exp(t_0 / [FVC - 1]) \quad (13)$$

where FVC denotes vegetation coverage (0–1), while  $C_0$  and  $t_0$  serve as fitting parameters, each assigned values of 2.2 and 48.54, respectively. The fitting determination coefficient  $R^2$  stands at 0.99.

#### 4.4. Recommendations for the Implementation of Sand Control Measures in the Future

Based on the aforementioned and previous research findings, it is indeed necessary to implement sand-control measures to ensure the sustainable operation of the newly constructed Oshang Railway. We have summarized some recommendations as follows:

For areas prone to significant sand transport such as Brickwell, Baga Zhoulegai, and Amuleng, where the angle between the main sand transport direction and the railway line is small, we suggest employing zig-zag-shaped sand barriers [17,18] for perimeter sand prevention. Utilizing two to three layers of sand barriers [18,19,25] is preferable, as this configuration can effectively contain blown sand within the barrier system.

In areas with minor sand transport like Sandaoquanzi Village and Liujiawan, where the angle between the main sand transport direction and the railway line exceeds  $51^\circ$ , upright

sand barriers are recommended for sand prevention. It is advisable to install one to two layers of upright sand barriers [19,25] perpendicular to the main sand transport direction.

Regarding fractional vegetation cover, maintaining a sparse vegetation cover of at least 20% can effectively inhibit the development of blown sand. We suggest planting sparse grass vegetation between sand barriers and the railway line to resist blown sand effectively. This planting method [45] can efficiently impede blown sand development without compromising environmental capacity and can also reduce planting costs.

Implementing these suggestions should contribute to reasonably safeguarding the sustainable operation of the railway and mitigating the impact of blown sand disasters to some extent.

## 5. Conclusions

This paper displays the spatial characteristics of blown sand transport along the Oshang Railway via field observation and utilizes an empirical expression to quantitatively assess sand transport under varying vegetation cover. This not only lends support to the implementation of wind and sand protection systems along the railway, providing essential reference data for the sustainable management of wind and disasters along the railway line and the preservation of regional environments but also contributes to the advancement of foundational research in aeolian physics. The findings of this study are as follows:

1. Sandaoquanzi Village, Amuleng, and Baga Zhoulegai areas along the railway are categorized as high wind energy environments, while Brickwell is classified as medium and Liujiawan as low. The Baga Zhoulegai area experiences minimal changes in wind direction, predominantly from the west to southwest, whereas other observation sites encounter significant directional variations.
2. The intensity of sand transport along the railway diminishes in the Brickwell, Baga Zhoulegai, Amuleng, Sandaoquanzi Village, and Liujiawan areas, with values of 303.70 kg/(m·a), 228.61 kg/(m·a), 102.94 kg/(m·a), 5.81 kg/(m·a), and 5.4 kg/(m·a), respectively. Similarly, the intensity of sand transport perpendicular to the railway decreases in these areas, with values of 88.7 kg/(m·a), 72.1 kg/(m·a), 25.95 kg/(m·a), 3.78 kg/(m·a), and 0.93 kg/(m·a), respectively. Moreover, the intensity of sand transport decreases in Brickwell, Baga Zhoulegai, Amuleng, Liujiawan, and Sandaoquanzi parallel to the direction of the railway, with values of 199.1 kg/(m·a), 187.6 kg/(m·a), 75.36 kg/(m·a), 0.82 kg/(m·a), and 0.26 kg/(m·a), respectively. When implementing sand control measures along the railway, it is crucial to consider both perpendicular and parallel wind-sand transport directions relative to the railway.
3. The dimensionless ratio of sand transport rate ( $Q$ ) to drift potential ( $DP$ ) on a flat surface follows a negative exponential trend with increasing normalized fractional vegetation cover ( $FVC$ ). When the vegetation cover exceeds 20% (vegetation cover threshold), it effectively mitigates the development of blown sand flux.
4. We offer recommendations for implementing sand protection measures along the Oshang Railway, adhering to the principle of “intensive protection for severe disasters and lighter protection for mild ones”. Our suggestion includes utilizing two to three layers of zigzag-shaped sand barriers in Brickwell, Baga Zhoulegai, and Amuleng areas, and one to two layers of high upright sand barriers in Sandaoquanzi Village and Liujiawan areas. Additionally, we propose planting sparse grass vegetation with a coverage rate exceeding 20% between the sand barriers and the railway to effectively suppress the development of blown sand.

**Author Contributions:** Conceptualization, N.H. and Y.S.; methodology, Y.S.; formal analysis, Y.S.; investigation, X.L.; resources, X.L. and B.H.; data curation, L.X.; writing—original draft preparation, Y.S.; writing—review and editing, J.Z.; supervision, J.Z.; project administration, J.Z.; funding acquisition, N.H. and X.L. All authors have read and agreed to the published version of the manuscript.

**Funding:** This research was funded by the National Natural Science Foundation of China (grant no. 41931179, 42376232), National key research and development program (2023YFF1304203), the Second

Tibetan Plateau Scientific Expedition and Research Program (grant no. 2019QZKK020611) and the Key Subjects of Science and Technology Development Program of China Railway Engineering Design and Consulting Group Co., Ltd. (Research-2019-62). We sincerely appreciate the financial support for these projects.

**Institutional Review Board Statement:** Not applicable.

**Informed Consent Statement:** Not applicable.

**Data Availability Statement:** The data presented in this study are available on request from the corresponding author.

**Conflicts of Interest:** Author Xuanmin Li was employed by the company China Railway Engineering Design and Consulting Group Co., Ltd. The remaining authors declare that the research was conducted in the absence of any commercial or financial relationships that could be construed as a potential conflict of interest.

## References

1. Sun, J.M.; Ding, Z.L.; Liu, T.S.; Rokosh, D.; Rutter, N. 580,000-year environmental reconstruction from aeolian deposits at the Mu Us Desert margin, China. *Quat. Sci. Rev.* **1999**, *18*, 1351–1364. [\[CrossRef\]](#)
2. Sun, J.M. Origin of aeolian sand mobilization during the past 2300 years in the Mu Us Desert, China. *Quat. Res.* **2000**, *53*, 78–88. [\[CrossRef\]](#)
3. Meaden, G.T.; Kochev, S.; Kolendowicz, L.; Kosa-Kiss, A.; Marciniene, I.; Sioutas, M.; Tyrrell, J. Comparing the theoretical versions of the Beaufort scale, the T-Scale and the Fujita scale. *Atmos. Res.* **2007**, *3*, 446–449. [\[CrossRef\]](#)
4. Wang, X.M.; Cheng, H.; Li, H.; Lou, J.P.; Hua, T.; Liu, W.B.; Jiao, L.L.; Ma, W.Y.; Li, D.F.; Zhu, B.Q. Key driving forces of desertification in the Mu Us Desert, China. *Sci. Rep.* **2017**, *7*, 3933. [\[CrossRef\]](#) [\[PubMed\]](#)
5. Sun, Z.H.; Mao, Z.A.; Yang, L.Y.; Liu, Z.; Han, J.C.; Wang, H.Y.; He, W. Impacts of climate change and afforestation on vegetation dynamic in the Mu Us Desert, China. *Ecol. Indic.* **2021**, *129*, 108020. [\[CrossRef\]](#)
6. Liu, J.K.; Bian, Z.; Zhang, K.B.; Ahmad, B.; Khan, A. Effects of different fencing regimes on community structure of degraded desert grasslands on Mu Us desert, China. *Ecol. Evol.* **2019**, *9*, 3367–3377. [\[CrossRef\]](#) [\[PubMed\]](#)
7. Cheng, J.J.; Jiang, F.Q.; Xue, C.X.; Xin, G.W.; Li, K.C.; Yang, Y.H. Characteristics of the disastrous wind-sand environment along railways in the Gobi area of Xinjiang, China. *Atmos. Environ.* **2015**, *102*, 344–354. [\[CrossRef\]](#)
8. Raffaele, L.; Bruno, L. Windblown sand action on civil structures: Definition and probabilistic modelling. *Eng. Struct.* **2019**, *178*, 88–101. [\[CrossRef\]](#)
9. Tang, G.D.; Meng, Z.J.; Gao, Y.; Dang, X.H. Impact of utility-scale solar photovoltaic array on the aeolian sediment transport in Hobq Desert, China. *J. Arid Land* **2021**, *13*, 274–289. [\[CrossRef\]](#)
10. Wu, X.G.; Fan, J.Q.; Sun, L.; Zhang, H.F.; Xu, Y.; Yao, Y.F.; Yan, X.D.; Zhou, J.; Jia, Y.S.; Chi, W.F. Wind erosion and its ecological effects on soil in the northern piedmont of the Yinshan Mountains. *Ecol. Indic.* **2021**, *128*, 107825. [\[CrossRef\]](#)
11. Bruno, L.; Horvat, M.; Raffaele, L. Windblown sand along railway infrastructures: A review of challenges and mitigation measures. *J. Wind Eng. Ind. Aerodyn.* **2018**, *177*, 340–365. [\[CrossRef\]](#)
12. Wang, J.C.; Song, Y.H.; Huang, N. Field Observation on the Spatial Characteristic of Wind-Blown Sand along the Hetian-Rouqiang Railway. *J. Phys. Conf. Ser.* **2023**, *2468*, 012174. [\[CrossRef\]](#)
13. Shi, L.; Wang, D.; Li, K. Windblown sand characteristics and hazard control measures for the Lanzhou–Wulumuqi high-speed railway. *Nat. Hazards* **2020**, *104*, 353–374. [\[CrossRef\]](#)
14. Xie, S.B.; Qu, J.J.; Lai, Y.M.; Pang, Y.J. Formation mechanism and suitable controlling pattern of sand hazards at Honglianghe River section of Qinghai–Tibet Railway. *Nat. Hazard.* **2015**, *76*, 855–871. [\[CrossRef\]](#)
15. Zhang, K.C.; Qu, J.J.; Liao, K.T.; Niu, Q.H.; Han, Q.J. Damage by wind-blown sand and its control along Qinghai–Tibet Railway in China. *Aeolian Res.* **2010**, *1*, 143–146. [\[CrossRef\]](#)
16. Dong, Z.B.; Chen, G.T.; He, X.D.; Han, Z.W.; Wang, X.M. Controlling blown sand along the highway crossing the Taklimakan Desert. *J. Arid. Environ.* **2004**, *57*, 329–344. [\[CrossRef\]](#)
17. Eichmanns, C.; Schüttrumpf, H. Investigating changes in Aeolian sediment transport at coastal dunes and sand trapping fences: A field study on the German coast. *J. Mar. Sci. Eng.* **2020**, *8*, 1012. [\[CrossRef\]](#)
18. Eichmanns, C.; Lechthaler, S.; Zander, W.; Pérez, M.V.; Blum, H.; Thorenz, F.; Schüttrumpf, H. Sand trapping fences as a nature-based solution for coastal protection: An international review with a focus on installations in Germany. *Environments* **2021**, *8*, 135. [\[CrossRef\]](#)
19. Li, B.L.; Sherman, D.J. Aerodynamics and morphodynamics of sand fences: A review. *Aeolian Res.* **2015**, *17*, 33–48. [\[CrossRef\]](#)
20. Miller, D.L.; Thetford, M.; Yager, L. Evaluation of sand fence and vegetation for dune building following overwash by Hurricane Opal on Santa Rosa Island, Florida. *J. Coastal Res.* **2001**, *17*, 936–948.
21. Levin, N.; Ben-Dor, E.; Kidron, G.J.; Yaakov, Y. Estimation of surface roughness ( $z_0$ ) over a stabilizing coastal dune field based on vegetation and topography. *Earth Surf. Process. Landf.* **2008**, *33*, 1520–1541. [\[CrossRef\]](#)



22. Grafals-Soto, R. Understanding the Effects of Sand Fence Usage and the Resulting Landscape, Landforms and Vegetation Patterns: A New Jersey Example. Ph.D. Thesis, Rutgers University-Graduate School, New Brunswick, NJ, USA, 2010.
23. Wang, T.; Qu, J.J.; Ling, Y.Q.; Liu, B.L.; Xiao, J.H. Shelter effect efficacy of sand fences: A comparison of systems in a wind tunnel. *Aeolian Res.* **2018**, *30*, 32–40. [\[CrossRef\]](#)
24. Lima, I.A.; Araújo, A.D.; Parteli, E.J.; Andrade, J.S.; Herrmann, H.J. Optimal array of sand fences. *Sci. Rep.* **2017**, *7*, 45148. [\[CrossRef\]](#) [\[PubMed\]](#)
25. Ma, B.T.; Gao, L.; Cheng, J.J.; Ding, B.S.; Ding, L.S.; Qu, L.; An, Y.F. Characteristics and Hazards of an Aeolian Sand Environment along Railways in the Southeastern Fringe of the Taklimakan Desert and Sand Control Measures. *Appl. Sci.* **2022**, *12*, 9186. [\[CrossRef\]](#)
26. Gillies, J.A.; Etyemezian, V.; Nikolich, G.; Glick, R.; Rowland, P.; Pesce, T.; Skinner, M. Effectiveness of an array of porous fences to reduce sand flux: Oceano Dunes, Oceano CA. *J. Wind Eng. Ind. Aerodyn.* **2017**, *168*, 247–259. [\[CrossRef\]](#)
27. Cheng, J.J.; Lei, J.Q.; Li, S.Y.; Wang, H.F. Disturbance of the inclined inserting-type sand fence to wind–sand flow fields and its sand control characteristics. *Aeolian Res.* **2016**, *21*, 139–150. [\[CrossRef\]](#)
28. Ning, Q.Q.; Li, B.L.; Ellis, J.T. Fence height control on sand trapping. *Aeolian Res.* **2020**, *46*, 100617. [\[CrossRef\]](#)
29. Hotta, S.; Horikawa, K. Function of sand fence placed in front of embankment. In *Coastal Engineering 1990*; ASCE Library: Reston, VA, USA, 2015; pp. 2754–2767. [\[CrossRef\]](#)
30. Zhang, K.; Zhao, P.W.; Zhao, J.C.; Zhang, X.X. Protective effect of multi-row HDPE board sand fences: A wind tunnel study. *Int. Soil Water Conserv. Res.* **2021**, *9*, 103–115. [\[CrossRef\]](#)
31. Itzkin, M.; Moore, L.J.; Ruggiero, P.; Hacker, S.D. The effect of sand fencing on the morphology of natural dune systems. *Geomorphology* **2020**, *352*, 106995. [\[CrossRef\]](#)
32. Zhang, K.; Tian, J.J.; Qu, J.J.; Zhao, L.M.; Li, S. Sheltering effect of punched steel plate sand fences for controlling blown sand hazards along the Golmud-Korla Railway: Field observation and numerical simulation studies. *J. Arid Land* **2022**, *14*, 604–619. [\[CrossRef\]](#)
33. Fryberger, S.G.; Dean, G. *A Study of Global sand Seas*; US Government Printing Office: Washington, DC, USA, 1979; Volume 1052, pp. 137–169.
34. Pye, K.; Tsaoar, H. *Aeolian Sand and Sand Dunes*; Springer Science & Business Media: Berlin/Heidelberg, Germany, 2008.
35. Huang, N.; Song, Y.H.; Xu, L.H.; Kuang, Q.; Chen, J.; Liu, C.; Xie, J.Y.; Xin, G.W.; Zhang, J. The Method for Quantitative Assessment of Sand-Drift Rate along the Southeastern Fringe of the Taklimakan Desert. *J. Environ. Account. Manag.* **2024**, *12*, 27–45. [\[CrossRef\]](#)
36. Wasson, R.J.; Nanninga, P.M. Estimating wind transport of sand on vegetated surfaces. *Earth Surf. Process. Landf.* **1986**, *11*, 505–514. [\[CrossRef\]](#)
37. Lyles, L.; Allison, B.E. Wind erosion: The protective role of simulated standing stubble. *Trans. Asae. Am Soc. Agric. Eng.* **1976**, *19*, 61–64. [\[CrossRef\]](#)
38. Marshall, J.K. Assessing the protective role of shrub-dominated rangeland vegetation against soil erosion by wind. In Proceedings of the 11th International Grassland Congress, Surfers Paradise, Australia, 11–23 April 1970; pp. 19–23.
39. Casado, M.A.; Castro, I.; Ramírez-Sanz, L.; Costa-Tenorio, M.; Miguel, J.M.D.; Pineda, F.D. Herbaceous plant richness and vegetation cover in mediterranean grasslands and shrublands. *Plant Ecol.* **2004**, *170*, 83–91.
40. Sun, H.T. *A Numerical Study on the Characteristics of Wind-Blown Sand over Discontinuous Crust Surface*; Lanzhou University: Lanzhou, China, 2023; p. 62. (In Chinese)
41. Bagnold, R.A. *The Physics of Blown Sand and Desert Dunes*; Dover Publications: Methuen, NY, USA, 1941. [\[CrossRef\]](#)
42. Wu, Z. *Wind and Sand Geomorphology*; Science Press: Beijing, China, 1987. (In Chinese)
43. Hoonhout, B.M.; Vries, S.D. A process-based model for aeolian sediment transport and spatiotemporal varying sediment availability. *J. Geophys. Res. Earth Surface* **2016**, *121*, 1555–1575. [\[CrossRef\]](#)
44. TB 10035-2018; Code for Design on Special Railway Earth Structure: State Railway Administration (PRC): Beijing, China, 2018; p. 96.
45. Liu, D.Y.; Feng, W.; Wang, T.; Yang, W.B.; Zhu, B.; Zou, H.; Zhou, M. Characteristics of vegetation restoration based on the theory of low vegetation coverage for desertification control. *J. Desert Res.* **2024**, *44*, 170–177. (In Chinese)
46. Benesty, J.; Chen, J.; Huang, Y.; Cohen, I. Pearson correlation coefficient. In *Noise Reduction in Speech Processing*; Springer: Berlin/Heidelberg, Germany, 2009; pp. 1–4.
47. Brophy, A.L. An algorithm and program for calculation of Kendall's rank correlation coefficient. *Behav. Res. Methods Instrum. Comput.* **1986**, *18*, 45–46. [\[CrossRef\]](#)
48. Gauthier, T.D. Detecting trends using spearman's rank correlation coefficient. *Environ. Forensics* **2001**, *2*, 359–362. [\[CrossRef\]](#)
49. Duan, S.Z.; Cheng, N.; Xie, L. A new statistical model for threshold friction velocity of sand particle motion. *Catena* **2013**, *104*, 32–38. [\[CrossRef\]](#)
50. Kawamura, R. Study on sand movement by wind. *Tokyo Univ. Inst. Sci. Technol. Rep.* **1951**, *5*, 95–112.
51. Neuman, M.; Nickling, W.G. A theoretical and wind tunnel investigation of the effect of capillary water on the entrainment of sediment by wind. *Can. J. Soil Sci.* **1989**, *69*, 79–96. [\[CrossRef\]](#)
52. Lancaster, N.; Baas, A. Influence of vegetation cover on sand transport by wind: Field studies at Owens Lake, California. *Earth Surf. Process. Landf. J. Br. Geomorphol. Group* **1998**, *23*, 69–82. [\[CrossRef\]](#)



- 
53. Buckley, R. The effect of sparse vegetation on the transport of dune sand by wind. *Nature* **1987**, *325*, 426–428. [[CrossRef](#)]
  54. Lettau, K.; Lettau, H.H. *Experimental and Micrometeorological Field Studies of Dune Migration, Exploring in the World's Driest Climate*; IES Report 101; University of Wisconsin-Madison: Madison, WI, USA, 1978; pp. 110–147. [[CrossRef](#)]

**Disclaimer/Publisher's Note:** The statements, opinions and data contained in all publications are solely those of the individual author(s) and contributor(s) and not of MDPI and/or the editor(s). MDPI and/or the editor(s) disclaim responsibility for any injury to people or property resulting from any ideas, methods, instructions or products referred to in the content.